PAPER

Spin current nano-oscillator (SCNO) as a potential frequency-based, ultra-sensitive magnetic biosensor: a simulation study

To cite this article: Renata Saha *et al* 2020 *Nanotechnology* **31** 375501

IOP Publishing Nanotechnology

Nanotechnology **31** (2020) 375501 (9pp) https://doi.org/10.1088/1361-6528/ab9921

Spin current nano-oscillator (SCNO) as a potential frequency-based, ultra-sensitive magnetic biosensor: a simulation study

Renata Saha[1], **Kai Wu**[1], **Diqing Su**[2] and **Jian-Ping Wang**[1]

[1] Department of Electrical and Computer Engineering, University of Minnesota, Minneapolis, MN 55455, United States of America
[2] Department of Chemical Engineering and Material Science, University of Minnesota, Minneapolis, MN 55455, United States of America

E-mail: wuxx0803@umn.edu and jpwang@umn.edu

Received 14 April 2020, revised 22 May 2020
Accepted for publication 3 June 2020
Published 30 June 2020

Abstract

This work is a micromagnetic simulation-based study on the GHz-frequency ferromagnetic resonances (FMR) for the detection of magnetic nanoparticles (MNPs) using spin current nano-oscillator (SCNO) operating in precession mode. Capture antibody-antigen-detection antibody-MNP complex on the SCNO surface generates magnetic fields that modify the FMR peaks and generate measurable resonance peak shifts. Moreover, our results strongly indicate the position-sensitive behavior of the SCNO biosensor and demonstrate ways to eradicate this effect to facilitate improved bio-sensing. Additionally, a study has been made on how MNPs with different sizes can alter the SCNO device performance. This simulation-based study on the SCNO device shows the feasibility of a frequency-based nano-biosensor with the sensitivity of detecting a single MNP, even in presence of background noise.

Supplementary material for this article is available online

Keywords: spin current nano-oscillator (SCNO), magnetic nanoparticles (MNPs), single molecule sensitivity, position sensitive behavior, frequency-based nanobiosensor, spintronic nanodevice, target antibody-antigen-capture antibody-MNP complex

(Some figures may appear in colour only in the online journal)

1. Introduction

It has been two decades since Baselt *et al* [1] had designed the bead array counter (BARC) that first showed the experimental possibility of bio-detection for multilayer giant magnetoresistance (GMR) with magnetic nanoparticles (MNPs) as biomarkers. Since then, magnetic biosensing for point-of-care (POC) detection of diseases using magnetoresistance (MR) sensors [2–13] have been explored and reviewed intensively [14–16]. In comparison to the other traditional biosensors reported such as optical-based sensors [17–23], the GMR sensors exhibit lower background noise. This is due to the fact that biomedical samples exhibit negligible magnetic background which in turn suppresses noise from the cellular matrix to a great extent [24], enabling detection of a single magnetic bead [25, 26]. The presence of MNP(s) cause variation in the static magnetic configuration of the sensor, altering the device resistance.

However, these MR sensors tend to suffer from high background noise levels at room temperature which compromises the sensitivity of the device. Until recently, ferromagnetic resonance (FMR)-based homogeneous and volumetric detection of deoxyribonucleic acid (DNA) was reported by Tian *et al* [27] where the binding of *V. cholerae* target DNA sequence led to aggregation of MNPs. This gave rise to a significant FMR

peak shift when compared to a non-aggregated MNP sample. In this kind of biosensing, they inserted the MNP samples inside an electromagnet cavity and took the readouts. In the nanoscale level, no such investigation of real-time frequency-based biosensing has been reported till date. It was Peter Metaxas's group from University of Western Australia who for the first time reported a possibility of such nanoscale frequency-based biosensing scheme. But all of their simulations as well as experimental studies were limited to detection of MNPs through oscillations on magnonic crystals (MCs) [28, 29], ferromagnetic nanodots [30] and/or nanodiscs [31]. At the nanoscale, the FMR frequency of the device interacts directly with the stray field(s) of the MNP(s) [32] and causes a shift in the peak frequency of the device. The advantage of a frequency-based, dynamic approach over the static MR-based sensing is that the device response is linear over a large range of the externally applied magnetic field leading to enhanced accuracy [33–35]. This frequency is typically in the order of several GHz, which is way too high as compared to the low frequency 1/f noise, and hence devoid of DC voltage-level drift.

In this regard, spin torque nano-oscillators (STNO) [33, 36–39] driven by spin transfer torque (STT) [40, 41] deserve special mention [42]. The stack structure being similar to a spin-valve, the spin-polarized electric current passing through a thin ferromagnetic (FM) layer dynamically excites the magnetic moment of the FM layer through the transfer of spin angular momentum. However, STNO devices are limited by consumption of large currents as the electrons by a total angular momentum of $\hbar/2$ [43]. Furthermore, higher the magnetic moment, higher is the current required to operate. But the positive trade-off is that it yields greater thermal stability with higher magnetic moment. In-plane magnetized spin Hall nano-oscillators (SHNO) [43–50] consisting of a heavy metal (HM)/FM stack do not have that limitation of angular momentum as constant scattering takes place at the HM/FM interface. Besides, no electron is required to flow through the active FM. Consequently, unpredicted damage due to electromigration and ohmic heating is prevented in spin Hall effect (SHE) devices [47, 48, 51]. Unlike STT, SHE supports magneto-optical measurements in direct contact with the active area of the device. From fabrication point-of-view, SHNOs are also easier to fabricate.

SHNOs with perpendicular magnetized anisotropy (PMA) are not feasible as was theoretically proved by Tomohiro Taniguchi [52]. The spin-orbit torque (SOT) effects from the heavy metal (HM) and perpendicularly magnetized ferromagnetic layer (PMA-FM) bilayer system contribute to the current-induced phenomena including the SHE, the Rashba effect [53], the DMI [54] etc. A combination of all these interactions contribute to a more stable oscillator system than the in-plane magnetized SHNOs. The possibility of inducing dynamical states of HM/FM bilayer or altering their static configuration by the current-induced spin torque [40, 41] that has triggered extensive experimental and theoretical research. In this respect, a promising approach is the PMA-SCNO [55] devices with an in-plane externally applied magnetic field and current. However, the investigation of SCNOs in terms of frequency-based nano-biosensors have not been reported.

In this research work, we investigate the feasibility of SCNO device as a frequency-based spintronic biosensor through micromagnetic simulations on Mumax3 [56] and point out its advantages and disadvantages and demonstrate ways to eradicate them. As per our best knowledge, none of these spintronic nano-oscillators have been investigated as potential frequency-based biosensors. For experimental validation of these SCNO biosensors there are several points of concern. First, these nano-oscillator arrays are required to be synchronized. Several synchronization techniques of these nano-oscillators have been investigated either through experiments [47, 48, 57, 58] or through theoretical [59, 60] approaches. Second, the frequency of oscillation of these nano-oscillators are in the GHz frequency range. This specific frequency range encourages significant water absorption and scattering [61]. Every biomedical sample contains an aqueous part. Therefore, after the MNP-detection antibody-antigen-capture antibody sandwich complex binding event on the SCNO surface, one needs to air-dry the sample to remove any aqueous component. This also explains why drying of the samples after the binding event was an extremely important step in the experiments to demonstrate frequency-based biosensing by magnonic crystals (MCs) [28, 29], ferromagnetic nanodots [30] and/or nanodiscs [31]. Finally, as these nano-oscillators are of the dimensions of several nanometers and the size of the antibodies is about 10 nm, extremely precise control over printing of these capture antibodies on the SCNO sensor surface is required. This work is a proof-of-concept as to the advantages of spintronic nano-oscillators as a potential frequency-based biosensor as will be discussed in the following sections. Since this is a simulation-based study, an elaborative discussion on experimental demonstration has been restricted. This paper has been organized as follows: In section 2, the schematic model of the proposed SCNO biosensor and the simulation parameters associated with the modeling has been demonstrated. In section 3, a detailed explanation of the device performance from the viewpoint of a bare device to that of a regularly and irregularly spaced MNPs have been made. In section 3.3, the effect of the size of MNPs on the SCNO biosensor performance has been made. In section 4, the room temperature, single molecular sensitivity of the SCNO biosensor has been demonstrated. Finally, in section 5, concluding remarks and summary of the proposed SCNO biosensor has been made.

2. Modeling and simulation

The SCNO device has been simulated numerically by solving the Landau–Lifshitz–Gilbert (LLG) equation (1) in addition to SOT term:

$$\frac{d\boldsymbol{m}}{dt} = \gamma_0 \boldsymbol{h}_{eff} \times \boldsymbol{m} + \alpha \boldsymbol{m} \times \frac{d\boldsymbol{m}}{dt} + \frac{u}{t}\boldsymbol{m} \times (\boldsymbol{m}_p \times \boldsymbol{m}), \qquad (1)$$

where, $\boldsymbol{m} = \boldsymbol{M}/M_s$ is the normalized magnetization, $\gamma_0 = 1.85 \times 10^{11}\,\mathrm{rad\,T^{-1}\,s^{-1}}$ is the gyromagnetic ratio, $\boldsymbol{h}_{\mathrm{eff}} = \boldsymbol{H}_{\mathrm{eff}}/M_s$ is the reduced effective field, t is the thickness of the FM layer, $\boldsymbol{m}_p$ is the current polarization vector, $u = \gamma_0 \left(\frac{\hbar jP}{2eM_s}\right)$,

Table 1. Micromagnetic simulation parameters.

Parameters	Description	FM nanopillar [62]	MNP(s) [63]
$\boldsymbol{\alpha}$	Gilbert damping factor	0.015	0.1
$\mathbf{A_{ex}}$	Exchange constant	13×10^{-12} J m^{-1}	2.64×10^{-11} J m^{-1}
$\boldsymbol{P}$	Electrical current polarization	0.6	NA
$\boldsymbol{M_s}$	Saturation magnetization	1200 kA m^{-1}	350 kA m^{-1}
$\boldsymbol{Ku_1}$	Uniaxial anisotropy	0.7×10^{6} J m^{-3}	1.25×10^{4} J m^{-3}
DMI	Dzyaloshinskii-Moriya interaction	0.7×10^{-4} J m^{-2}	NA

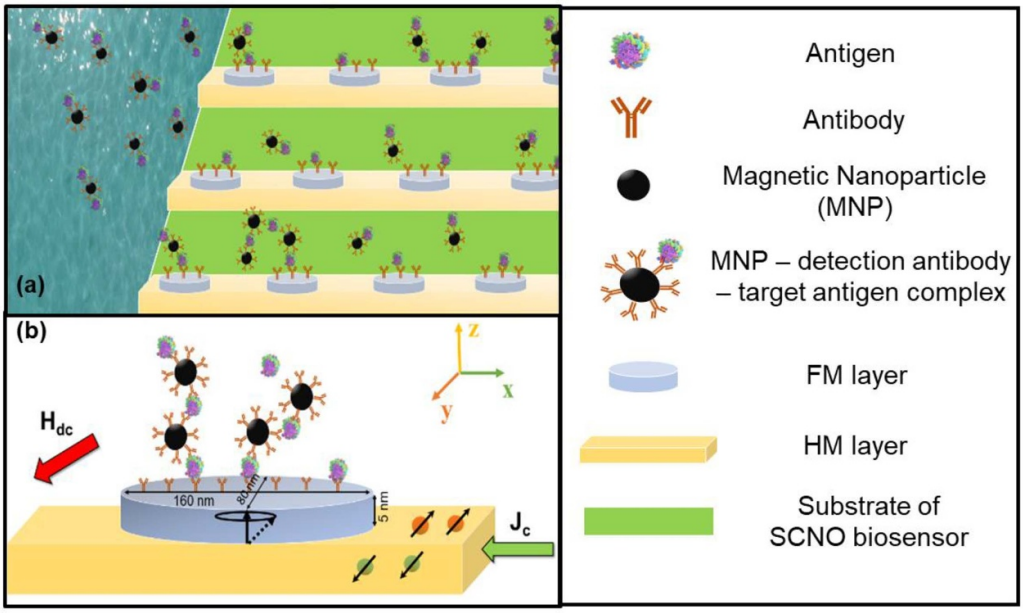

Figure 1. (a) Schematic of the SCNO biosensor array with the sandwich mechanism of capture antibody-target antigen-detection antibody-MNP complex demonstrated. (b) A single PMA-FM nanopillar of the SCNO biosensor array zoomed in. The black-dashed arrow in the ferromagnetic nanopillar demonstrates precession mode operation.

j is the density of the spin current, $\hbar$ is the reduced Planck's constant ($\hbar = 1.054571817 \times 10^{-34}$ Js and e is the fundamental charge of an electron ($e = 1.602 \times 10^{-19}$C). All parameters for simulation that define the FM layer and the MNPs are adopted from [62] and [63] respectively (Table 1).

For a bilayer of PMA-FM and HM, under an externally applied current and uniform DC magnetic field, the device operates in precession mode. It is with a precession frequency that the bare SCNO device oscillates, referred to in this work as the 'peak frequency' or the frequency which has maximum intensity.

Figure 1(a) gives a schematic view of the SCNO array with the FM nanopillar of dimensions 160 nm × 80 nm × 5 nm located 0.5 μm apart such that the stray fields of adjacent PMA-FM nanopillars do not influence the device performance (see supplementary material S2 (available online at stacks.iop.org/NANO/31/375501/mmedia)). Figure 1(a) also shows the mechanism in which the SCNO would facilitate magnetic biosensing through formation of capture antibody-antigen-detection antibody-MNP complex (sandwich structure). On applying a charge current ($\mathbf{J_c}$, A m^{-2}) through the HM layer along **-x** direction, it causes spin accumulation along $\pm$**y** and generation of a spin current along **z** direction (see figure 1(b)). When a magnetic field ($\mathbf{H_{dc}}$, Oe) is externally applied along **+y** direction, the spin current causes the FM nanopillar to operate in precession. The effects of a reversed direction of $\mathbf{J_c}$ and $\mathbf{H_{dc}}$ on SCNO device performance are given in supplementary material S1. The color and symbol codes for antigen, antibody, MNP, MNP- capture antibody—antigen complex, FM layer, HM layer & substrate of the SCNO used throughout in this work are specified in figure 1. Although the performance of SCNO biosensor has been reported at T = 0 K [64], discussion on thermal effects have been made in section 4.

3. Results and discussion

3.1. Device operation

For H_{dc} = 1.1 kOe in figure 2(a) the peak frequency for the SCNO biosensor changes with a variation of HM current. As reported previously, for in-plane SHNO [43, 44], a constant magnetic field with increase in current, decreases the peak frequency while the intensity of the main frequency component of the SCNO device increases (see figure 2(b)). Again, at constant current of i = 15 mA, but for varying DC magnetic field,

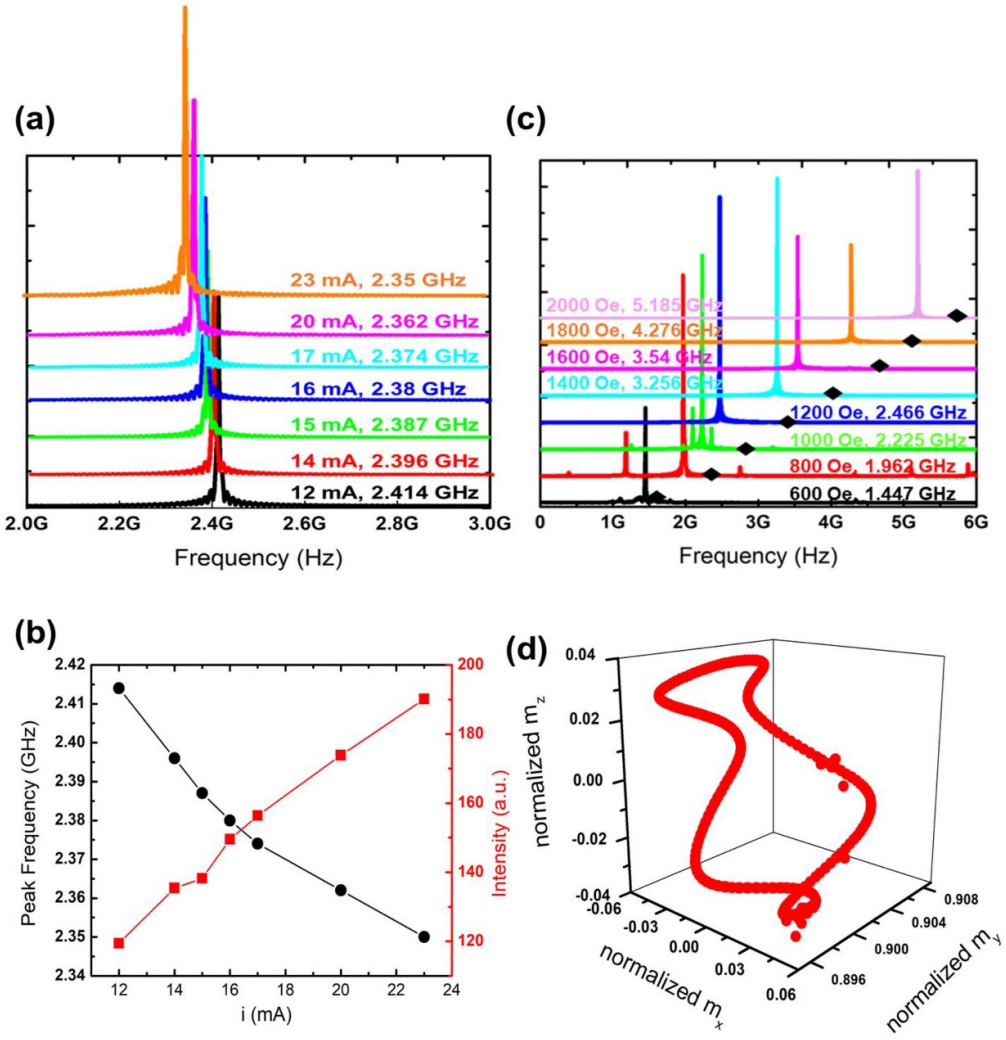

Figure 2. (a) Variation of peak frequency shift of a SCNO biosensor with current at $H_{dc} = 1.1$ kOe. (b) Variation of intensity (in a.u.) and magnitude of peak frequency with current for $H_{dc} = 1.1$ kOe. (c) Variation of the peak frequency with H_{dc} at i = 15 mA. The black diamonds represent the value of the FMR at the corresponding frequency calculated by the Kittel Equation. (d) The magnetization vector trajectory due to their precessional motion due to i = 15 mA and $H_{dc} = 1.1$ kOe.

we observe a clear increase in the peak frequency value in figure 2(c). This kind of peak frequency shift with increase in the static external magnetic field agrees with previously reported results in [45, 55]. The black diamonds represent the calculated ferromagnetic resonance frequency (f_{FMR}) value for a particular externally applied magnetic field as calculated by the normal magnetization Kittel Equation for in-plane magnetic field, $f_{FMR} = \gamma\sqrt{H_{dc}\,(H_{dc} + 4\pi M_z)}$, γ being the gyromagnetic ratio and M_z being the magnetization of the free layer along z direction. As reported earlier [55], the precession frequency for the designed SCNO biosensor must lie below the calculated FMR frequency. The trajectory of the magnetization vectors ($\mathbf{m_x}$, $\mathbf{m_y}$ and $\mathbf{m_z}$) due to precessional motion of the FM nanopillar are shown in figure 2(d). A single crossover point [65, 66] for the magnetization vector trajectories in figure 2(d) clearly demonstrates that there are two dynamic modes or two frequencies of oscillation for the SCNO system. There is one big loop followed by another small loop. This suggests that of the two frequencies, one frequency at 2.387 GHz has an extremely high intensity (140 arbitrary units (a.u.)) while the other frequency at 7 GHz, has significantly low intensity (10 a.u.). The two different frequencies of oscillation for i = 15 mA and $H_{dc} = 1.1$ kOe have been demonstrated in supplementary material S5. The peak with the higher intensity will be used for biosensing purpose.

3.2. *Effect of position of MNPs on the sensor*

In figure 3, a SCNO device devoid of any MNP positioned on the sensor surface has been termed as the 'bare' SCNO device. Figure 3(a) shows 5 independent positions of a single MNP: (i) = (0, 0), (ii) = (40, 20), (iii) = (−40, 20), (iv) = (−40, −20), (v) = (40, −20). Figure 3(b) correspond to 4 independent positions of 6 MNPs, each spaced regularly at 30 nm apart: (i) = first, (ii) = second, (iii) = third, (iv) = fourth quadrants. Figure 3(c) corresponds to 8 and 10 MNPs positioned at the center of the SCNO biosensor at similar spacing. All MNPs are identical with diameter of 20 nm and are defined

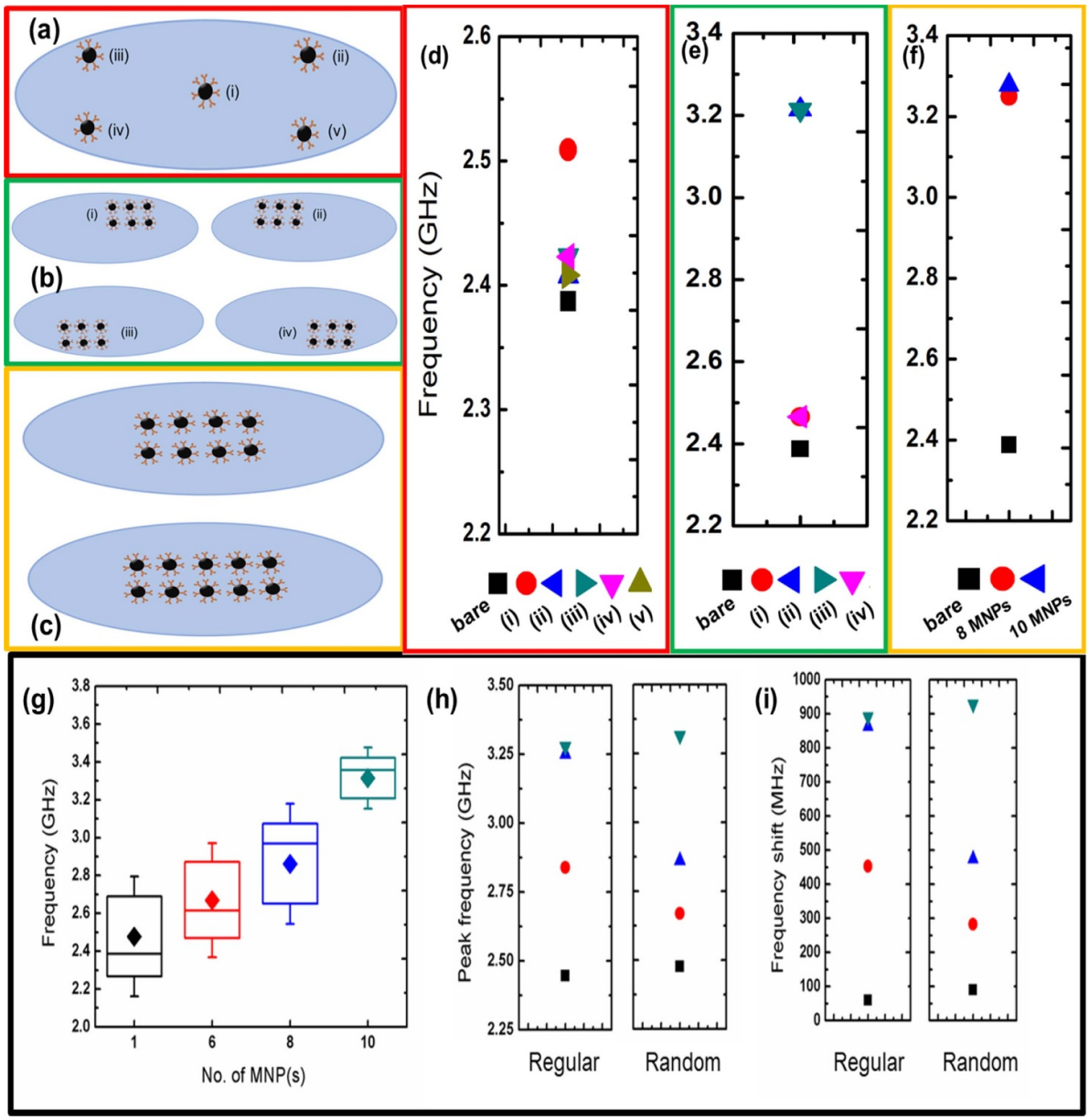

Figure 3. Schematic top view of the FM nanopillar containing (a) single MNP at positions marked (i), (ii), (iii), (iv) and (v). (b) 6 MNPs at 4 positions marked (i), (ii), (iii) and (iv). (c) 8 MNPs and 10 MNPs positioned at the center. (d), (e) & (f) Peak frequency for MNP positions demonstrated in (a), (b) & (c) respectively. (g) Peak frequencies for 1, 6, 8 and 10 no. of MNPs situated at random positions (n = 5). (h) Peak frequencies (in GHz) for regular and random positions. (i) The peak frequency shift (in MHz) for values in (h) from that of the bare SCNO device.

to be superparamagnetic in nature. Usually, when MNPs are used as biomarkers [16, 63, 67], they are superparamagnetic in nature. If they are not superparamagnetic, when one MNP-detection antibody-target antigen complex binds to the capture antibody on the sensor surface, the other MNPs are attracted by the remanence field of that MNP which has bonded to the surface.

The highlighted picture background color-codes corresponding to the peak frequencies for cases in figures 3(a), (b) & (c) have been displayed in figures 3(d), (e) & (f), respectively. Both figure 3(d) and (e) show that the peak frequency varies for different positions of the MNP(s). Furthermore, for both the cases of a single MNP and of 6 MNPs, the peak frequency for the positions in the first & fourth quadrant and for the positions in second & third quadrants are same. Therefore, the two halves of the SCNO device work differently due to unique magnetization distribution (see supplementary material S3). In figure 3(d) when the MNP is situated at the center, the frequency shift is higher from the bare device than when the MNPs are situated along the edges. Therefore, the SCNO biosensor is more sensitive at the center than along the two edges. Similarly, in figure 3(e), with the larger shift for 6 regularly spaced MNPs positioned in (ii) & (iii) as compared to (i) & (iv), it can be estimated that the left half of the SCNO sensor is more sensitive than its right half. Figure 3(f) demonstrates the case for 8 and 10 regularly spaced MNPs. In summary,

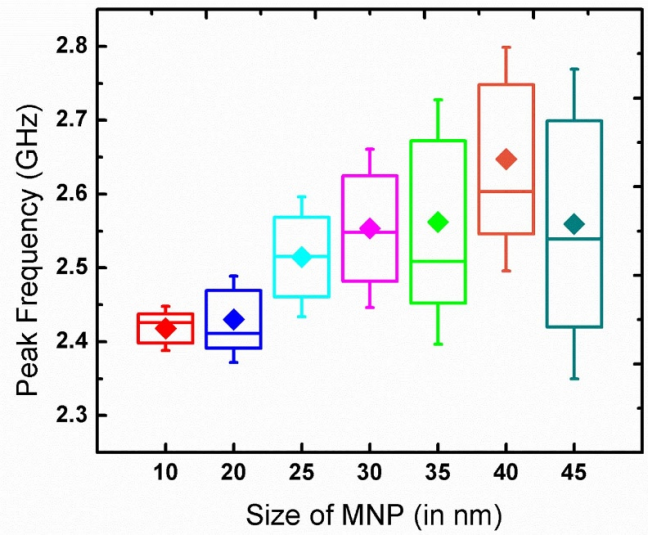

Figure 4. SCNO performance for varied sizes of a single MNP at random positions (n = 6) on the surface.

figure 3(a)–(f) validates the fact that SCNO biosensor performance is position specific, precisely, the two identical halves of the device work uniquely. As much as this position sensitivity of the designed SCNO biosensor is detrimental to biosensing performance for magnetic biosensors, one cannot deny the fact that the other magnetic biosensors, including the GMRs are position sensitive too. Analytical studies by Klein *et al* [68]. had shown how the edges of the GMR sensors are more sensitive towards detection of MNPs than the rest of the sensor stripe.

However, in real experiments [29, 30, 69], the MNPs are unlikely to be uniformly spaced as was the case in figures 3(a)–(c). To demonstrate a more realistic SCNO performance, we have further investigated the cases of 1, 6, 8 and 10 MNPs, but this time for 5 random arrangements on the SCNO surface for each number of MNPs. Figure 3(g) demonstrates the box-whisker plots for the peak frequencies of five cases of randomly positioned 1, 6, 8 and 10 MNPs, each. The mean values (colored diamonds) for 1, 6, 8 & 10 MNPs have been found to be 2.378 GHz, 2.556 GHz, 2.862 GHz and 3.314 GHz respectively. Furthermore, as the number of MNPs on the SCNO biosensor surface increases, the deviations decrease; the distance between the maximum and minimum points in the box–whisker plot decreases in each case of the number of MNP(s). Figure 3(h) shows the comparison of peak frequencies of regularly spaced 1, 6, 8 & 10 MNPs as discussed in figures 3(a)–(f) to that of the mean peak frequency values for randomly spaced 1, 6, 8 & 10 MNPs as discussed in figure 3(g). It is evident that for both regularly and randomly spaced MNPs, the peak frequency (in GHz) value increases with increase in number of the MNPs from 1, 6, 8 to 10 MNPs. This fact is validated from figure 3(h) by the shift in peak frequency (in MHz) from the bare SCNO device.

3.3. Effect of various sizes of MNPs

In figure 4, we have defined one MNP of 7 different diameters at random positions on the SCNO device surface. For 6 random positions on the SCNO device surface, MNPs of diameters, 10 nm, 20 nm, 25 nm, 30 nm, 35 nm, 40 nm and 45 nm show a mean peak frequencies 2.418 GHz, 2.43 GHz, 2.514 GHz, 2.554 GHz, 2.562 GHz, 2.647 GHz and 2.56 GHz, respectively. With increase in the diameter of the MNPs, the mean peak frequency increases gradually until at 45 nm where a sudden drop in mean peak frequency is observed. Analogous results for GMR signal level were experimentally observed by Wang *et al* [69]. for the purpose of GMR biosensing. Their reasoning for such kind of experimental observation was that between large and small size of MNPs, the latter encourages greater degree of Brownian motion [70] in experiments, which in turn facilitates greater diffusion and binding of the MNPs with the SCNO biosensor surface. Therefore, with increased diameter of the MNP, the binding tendency to the SCNO sensor surface decreases significantly thereby leading to a sudden drop in peak frequency.

4. Room temperature sensitivity of the SCNO biosensor

In the work, all the previous performance of the SCNO biosensor was demonstrated at T = 0 K. In figures 5(a) and (b) the performance of a bare SCNO device has been compared to that of the SCNO biosensor with a single MNP positioned at the center of the device in presence of thermal perturbation. It is a known fact that for room-temperature performance of magnetoresistive (MR) biosensors, the real-time sensitivity is highly compromised by background noise. Thus, to validate the fact that SCNO devices will perform better in this respect, some theoretical studies at different temperatures ranging from T = 0 K, 60 K, 200 K, 300 K, 400 K and 500 K have been carried out. The FFT peaks in figure 5(a) demonstrate that with the gradual increase in temperature, the intensity of the peaks for a bare SCNO device decreases implying the plot becomes noisy at 500 K but still the peaks are detectable. Figure 5(b) gives a detailed analysis of the intensity and peak frequency of the bare SCNO biosensor in comparison to that of a SCNO biosensor with a single MNP situated at the center. In both cases, with increase in temperature, the value of peak frequency increases but the intensity decreases significantly. This phenomenon is quite intuitive as with increase in surrounding temperature, the thermal effects increase significantly. This adds to the noisy background in the FFT data floor and the peaks become of comparable intensity to the background noise, thereby compromising the signal to noise (SNR) ratio. Thermal effects also significantly alter the magnetic properties. For instance, with increase in temperature, the saturation magnetization (M_s) of the ferromagnetic free layer increases [71]. Therefore, following Kittel Equation for in-plane magnetic field, $f_{FMR} = \gamma\sqrt{H_{dc}\,(H_{dc} + 4\pi M_z)}$, γ being the gyromagnetic ratio, H_{dc} being the external magnetic field and M_z is the magnetization along z direction ($M_z = \mathbf{m_z}{}^* M_s$). Hence, with increase in M_s with temperature, the FMR frequency increases. This justifies why we get a gradually increasing shift in the peak frequency value due to increase in temperature. It is evident that at T = 500 K, apart from the intensity (in a.u.) being low, there is no significant shift in frequency for

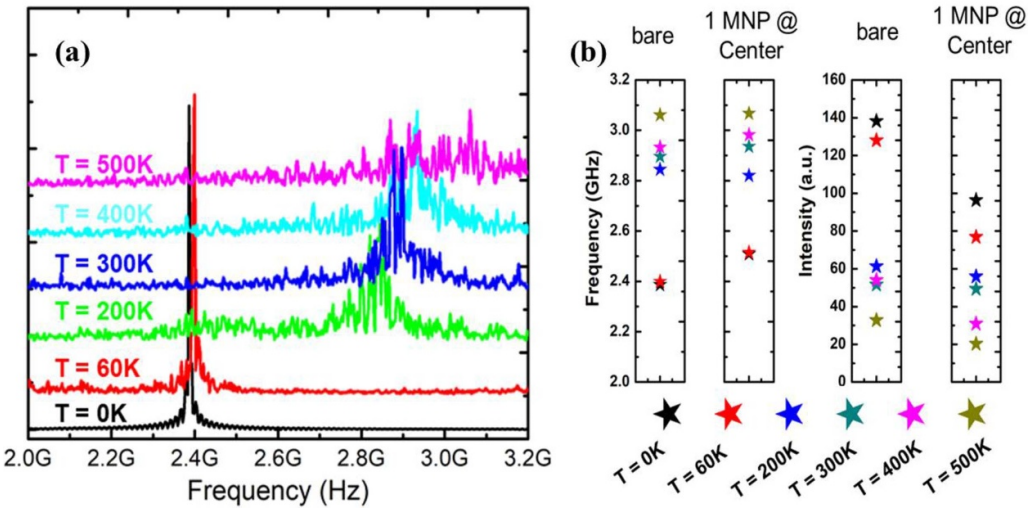

Figure 5. (a) Variation of the peak frequency of the SCNO biosensor at different temperature. It shows a prominent peak at T = 300 K. (b) Comparison of the peak frequency and the intensity at different temperatures for a bare sensor and a single MNP situated at the center of the MNP.

presence of a single MNP (f_{peak} = 3.067 GHz) in comparison to the frequency of a bare SCNO device (f_{peak} = 3.061 GHz).

It is unlikely that the real-time biosensing experiments using SCNO will be conducted at T = 500 K. At room temperature (T = 300 K), the difference in peaks for a bare SCNO device and a device with only a single MNP positioned at the center is discernible, both in terms of frequency and intensity (see figure 5(b); color-symbol code: cyan-stars). Figure 5 not only demonstrates good room temperature sensitivity of the SCNO biosensor but also demonstrates single molecular sensitivity of the SCNO biosensor at room temperature.

5. Conclusion

In conclusion, we have proposed and investigated the feasibility of a SCNO structure with PMA as a frequency-based biosensor. Through micromagnetic simulations, we have demonstrated that the SCNO biosensor has the sensitivity of detecting a single MNP and its performance varies with the position of the MNP on the sensor surface. However, with random position of the MNP(s), the position specific behavior of the SCNO biosensor can be eliminated to a great extent. Unlike MR sensors, the SCNO biosensor performance is not noisy at room temperature, yielding a more realistic device performance. Finally, in order to observe a distinct peak shift on addition of MNPs, a standard binding process is required to be initiated which demands an optimized selection of the size of the MNPs to be used as a biomarker.

Acknowledgments

This study was financially supported by the Institute of Engineering in Medicine (IEM) of the University of Minnesota through FY18 IEM Seed Grant Funding Program, the National Science Foundation MRSEC facility program, the Distinguished McKnight University Professorship, the Centennial Chair Professorship, and the Robert F Hartmann Endowed Chair from the University of Minnesota.

ORCID iDs

Renata Saha https://orcid.org/0000-0002-0389-0083
Kai Wu https://orcid.org/0000-0002-9444-6112
Diqing Su https://orcid.org/0000-0002-5790-8744
Jian-Ping Wang https://orcid.org/0000-0003-2815-6624

References

[1] Baselt D R, Lee G U, Natesan M, Metzger S W, Sheehan P E and Colton R J 1998 A biosensor based on magnetoresistance technology *Biosens. Bioelectron.* **13** 731–9
[2] Miller M, Prinz G, Cheng S-F and Bounnak S 2002 Detection of a micron-sized magnetic sphere using a ring-shaped anisotropic magnetoresistance-based sensor: a model for a magnetoresistance-based biosensor *Appl. Phys. Lett.* **81** 2211–3
[3] Rife J, Miller M, Sheehan P, Tamanaha C, Tondra M and Whitman L 2003 Design and performance of GMR sensors for the detection of magnetic microbeads in biosensors *Sensors Actuators Phys.* **107** 209–18
[4] Dittmer W, De Kievit P, Prins M, Vissers J, Mersch M and Martens M 2008 Sensitive and rapid immunoassay for parathyroid hormone using magnetic particle labels and magnetic actuation *J. Immunol. Methods* **338** 40–46
[5] Srinivasan B, Li Y, Jing Y, Xu Y, Yao X, Xing C and Wang J 2009 A detection system based on giant magnetoresistive sensors and high-moment magnetic nanoparticles demonstrates zeptomole sensitivity: potential for personalized medicine *Angew. Chem. Int. Ed.* **48** 2764–7
[6] Gaster R S, Xu L, Han S-J, Wilson R J, Hall D A, Osterfeld S J, Yu H and Wang S X 2011 Quantification of protein interactions and solution transport using high-density GMR sensor arrays *Nat. Nanotechnol.* **6** 314

[7] Marquina C, De Teresa J, Serrate D, Marzo J, Cardoso F, Saurel D, Cardoso S, Freitas P and Ibarra M 2012 GMR sensors and magnetic nanoparticles for immuno-chromatographic assays *J. Magn. Magn. Mater.* **324** 3495–8

[8] Aronoff-Spencer E, Venkatesh A, Sun A, Brickner H, Looney D and Hall D A 2016 Detection of Hepatitis C core antibody by dual-affinity yeast chimera and smartphone-based electrochemical sensing *Biosens. Bioelectron.* **86** 690–6

[9] Wu K, Klein T, Krishna V D, Su D, Perez A M and Wang J-P 2017 Portable GMR handheld platform for the detection of influenza A virus *ACS Sensors* **2** 1594–601

[10] Barroso T G, Martins R C, Fernandes E, Cardoso S, Rivas J and Freitas P P 2018 Detection of BCG bacteria using a magnetoresistive biosensor: a step towards a fully electronic platform for tuberculosis point-of-care detection *Biosens. Bioelectron.* **100** 259–65

[11] Su D, Wu K, Krishna V, Klein T, Liu J, Feng Y, Perez A M, Cheeran M C and Wang J-P 2019 Detection of influenza A virus in swine nasal swab samples with a wash-free magnetic bioassay and a handheld giant magnetoresistance sensing system *Front. Microbiol.* **10** 1077

[12] Ravi N, Rizzi G, Chang S E, Cheung P, Utz P J and Wang S X 2019 Quantification of cDNA on GMR biosensor array towards point-of-care gene expression analysis *Biosens. Bioelectron.* **130** 338–43

[13] Ng E, Yao C, Shultz T O, Ross-Howe S and Wang S X 2019 Magneto-nanosensor smartphone platform for the detection of HIV and leukocytosis at point-of-care *Nanomed. Nanotechnol. Biol. Med.* **16** 10–19

[14] Wang S X and Li G 2008 Advances in giant magnetoresistance biosensors with magnetic nanoparticle tags: review and outlook *IEEE Trans. Magn.* **44** 1687–702

[15] Llandro J, Palfreyman J, Ionescu A and Barnes C 2010 Magnetic biosensor technologies for medical applications: a review *Med. Biol. Eng. Comput.* **48** 977–98

[16] Wu K, Su D, Liu J, Saha R and Wang J-P 2019 Magnetic nanoparticles in nanomedicine: a review of recent advances *Nanotechnology* **30** 502003

[17] Chau Y-F C, C-t C C, Lim C M, Huang H J and Chiang H-P 2018 Depolying tunable metal-shell/dielectric core nanorod arrays as the virtually perfect absorber in the near-infrared regime *ACS Omega* **3** 7508–16

[18] Y-f C C, Chen K-H, Chiang H-P, Lim C M, Huang H J, Lai C-H and Kumara N 2019 Fabrication and characterization of a metallic–dielectric nanorod array by nanosphere lithography for plasmonic sensing application *Nanomaterials* **9** 1691

[19] Chau Y-F C 2020 Mid-infrared sensing properties of a plasmonic metal–insulator–metal waveguide with a single stub including defects *J. Phys. D: Appl. Phys.* **53** 115401

[20] Kumara N, Chau Y-F C, Huang J-W, Huang H J, Lin C-T and Chiang H-P 2016 Plasmonic spectrum on 1D and 2D periodic arrays of rod-shape metal nanoparticle pairs with different core patterns for biosensor and solar cell applications *J. Opt.* **18** 115003

[21] Chau Y-F, Jheng C-Y, Joe S-F, Wang S-F, Yang W, Jheng S-C, Sun Y-S, Chu Y and Wei J-H 2013 Structurally and materially sensitive hybrid surface plasmon modes in periodic silver-shell nanopearl and its dimer arrays *J. Nanopart. Res.* **15** 1424

[22] Y-f C C, C-t C C, Huang H J, Kumara N, Lim C M and Chiang H-P 2019 Ultra-high refractive index sensing structure based on a metal-insulator-metal waveguide-coupled T-shape cavity with metal nanorod defects *Nanomaterials* **9** 1433

[23] Chau Y-F C, Chao C-T C and Chiang H-P 2020 Ultra-broad bandgap metal-insulator-metal waveguide filter with symmetrical stubs and defects *Results Phys.* **17** 103116

[24] Colombo M, Carregal-Romero S, Casula M F, Gutiérrez L, Morales M P, Böhm I B, Heverhagen J T, Prosperi D and Parak W J 2012 Biological applications of magnetic nanoparticles *Chem. Soc. Rev.* **41** 4306–34

[25] Li G and Wang S X 2003 Analytical and micromagnetic modeling for detection of a single magnetic microbead or nanobead by spin valve sensors *IEEE Trans. Magn.* **39** 3313–5

[26] Liu Y, Jin W, Yang Y and Wang Z 2006 Micromagnetic simulation for detection of a single magnetic microbead or nanobead by spin-valve sensors *J. Phys. D: Appl. Phys.* **99** 08G102

[27] Tian B, Liao X, Svedlindh P, Strömberg M and Wetterskog E 2018 Ferromagnetic resonance biosensor for homogeneous and volumetric detection of DNA *ACS Sensors* **3** 1093–101

[28] Inoue M, Baryshev A, Takagi H, Lim P B, Hatafuku K, Noda J and Togo K 2011 Investigating the use of magnonic crystals as extremely sensitive magnetic field sensors at room temperature *Appl. Phys. Lett.* **98** 132511

[29] Pj M, Sushruth M, Ra B, Ding J, Rc W, Is M, Albert M, Wang W, Fangohr H and Ao A 2015 Sensing magnetic nanoparticles using nano-confined ferromagnetic resonances in a magnonic crystal *Appl. Phys. Lett.* **106** 232406

[30] Sushruth M, Ding J, Duczynski J, Woodward RC , Begley RA , Fangohr H, Fuller RO , Adeyeye AO , Kostylev M and Metaxas PJ 2016 Resonance-based detection of magnetic nanoparticles and microbeads using nanopatterned ferromagnets *Phys. Rev. Appl.* **6** 044005

[31] Albert M, Beg M, Chernyshenko D, Bisotti M-A, Carey R L, Fangohr H and Metaxas P J 2016 Frequency-based nanoparticle sensing over large field ranges using the ferromagnetic resonances of a magnetic nanodisc *Nanotechnology* **27** 455502

[32] Lee I, Obukhov Y, Xiang G, Hauser A, Yang F, Banerjee P, Pelekhov D V and Hammel P C 2010 Nanoscale scanning probe ferromagnetic resonance imaging using localized modes *Nature* **466** 845

[33] Braganca P, Gurney B, Wilson B, Katine J, Maat S and Childress J 2010 Nanoscale magnetic field detection using a spin torque oscillator *Nanotechnology* **21** 235202

[34] Petrie J, Urazhdin S, Wieland K, Fischer G and Edelstein A 2014 Using a spin torque nano-oscillator to read memory based on the magnetic permeability *J. Phys. Appl. Phys.* **47** 055002

[35] Rippard W H, Deac A M, Pufall M R, Shaw J M, Keller M W, Russek S E, Bauer G E and Serpico C 2010 Spin-transfer dynamics in spin valves with out-of-plane magnetized CoNi free layers *Phys. Rev.* B **81** 014426

[36] Kim J-V, Tiberkevich V and Slavin A N 2008 Generation linewidth of an auto-oscillator with a nonlinear frequency shift: spin-torque nano-oscillator *Phys. Rev. Lett.* **100** 017207

[37] Prokopenko O, Bankowski E, Meitzler T, Tiberkevich V and Slavin A 2011 Spin-torque nano-oscillator as a microwave signal source *IEEE Magn. Lett.* **2** 3000104–3000104

[38] Rowlands G E and Krivorotov I N 2012 Magnetization dynamics in a dual free-layer spin-torque nano-oscillator *Phys. Rev.* B **86** 094425

[39] Zheng C, Chen -H-H, Zhang X, Zhang Z and Liu Y 2019 Spin torque nano-oscillators with a perpendicular spin polarizer *Chin. Phys.* B **28** 037503

[40] Berger L 1996 Emission of spin waves by a magnetic multilayer traversed by a current *Phys. Rev.* B **54** 9353

[41] Slonczewski J C 1996 Current-driven excitation of magnetic multilayers *J. Magn. Magn. Mater.* **159** L1–7

[42] Xia H, Zheng Q, Mu C, Song C, Jin C, Liu Q and Wang J 2017 Micromagnetic simulation for detection of magnetic nanobeads by spin torque oscillator *J. Magn. Magn. Mater.* **432** 387–90

[43] Liu R, Lim W and Urazhdin S 2013 Spectral characteristics of the microwave emission by the spin Hall nano-oscillator *Phys. Rev. Lett.* **110** 147601

[44] Demidov V E, Urazhdin S, Ulrichs H, Tiberkevich V, Slavin A, Baither D, Schmitz G and Demokritov S O 2012 Magnetic nano-oscillator driven by pure spin current *Nat. Mater.* **11** 1028

[45] Ulrichs H, Demidov V and Demokritov S 2014 Micromagnetic study of auto-oscillation modes in spin-Hall nano-oscillators *Appl. Phys. Lett.* **104** 042407

[46] Ranjbar M, Drrenfeld P, Haidar M, Iacocca E, Balinskiy M, Le T, Fazlali M, Houshang A, Awad A and Dumas R 2014 CoFeB-based spin Hall nano-oscillators *IEEE Magn. Lett.* **5** 1–4

[47] Demidov V, Ulrichs H, Gurevich S, Demokritov S, Tiberkevich V, Slavin A, Zholud A and Urazhdin S 2014 Synchronization of spin Hall nano-oscillators to external microwave signals *Nat. Commun.* **5** 3179

[48] Awad A, Dürrenfeld P, Houshang A, Dvornik M, Iacocca E, Dumas R and Åkerman J 2017 Long-range mutual synchronization of spin Hall nano-oscillators *Nat. Phys.* **13** 292

[49] Demidov V, Urazhdin S, Zholud A, Sadovnikov A and Demokritov S 2014 Nanoconstriction-based spin-Hall nano-oscillator *Appl. Phys. Lett.* **105** 172410

[50] Zahedinejad M, Mazraati H, Fulara H, Yue J, Jiang S, Awad A and Åkerman J 2018 CMOS compatible W/CoFeB/MgO spin Hall nano-oscillators with wide frequency tunability *Appl. Phys. Lett.* **112** 132404

[51] Tarequzzaman M, Böhnert T, Decker M, Costa J, Borme J, Lacoste B, Paz E, Jenkins A, Serrano-Guisan S and Back C 2019 Spin torque nano-oscillator driven by combined spin injection from tunneling and spin Hall current *Commun. Phys.* **2** 20

[52] Taniguchi T 2015 Nonlinear analysis of magnetization dynamics excited by spin Hall effect *Phys. Rev.* B **91** 104406

[53] Bychkov Y A and Rashba E I 1984 Oscillatory effects and the magnetic susceptibility of carriers in inversion layers *J. Phys. C Solid State Phys.* **17** 6039

[54] Moriya T 1960 Anisotropic superexchange interaction and weak ferromagnetism *Phys. Rev.* **120** 91

[55] Liu R, Lim W and Urazhdin S 2015 Dynamical skyrmion state in a spin current nano-oscillator with perpendicular magnetic anisotropy *Phys. Rev. Lett.* **114** 137201

[56] Vansteenkiste A, Leliaert J, Dvornik M, Helsen M, Garcia-Sanchez F and Van Waeyenberge B 2014 The design and verification of MuMax3 *AIP Adv.* **4** 107133

[57] Urazhdin S, Tabor P, Tiberkevich V and Slavin A 2010 Fractional synchronization of spin-torque nano-oscillators *Phys. Rev. Lett.* **105** 104101

[58] Kaka S, Pufall M R, Rippard W H, Silva T J, Russek S E and Katine J A 2005 Mutual phase-locking of microwave spin torque nano-oscillators *Nature* **437** 389–92

[59] Georges B, Grollier J, Cros V and Fert A 2008 Impact of the electrical connection of spin transfer nano-oscillators on their synchronization: an analytical study *Appl. Phys. Lett.* **92** 232504

[60] Elyasi M, Bhatia C S and Yang H 2015 Synchronization of spin-transfer torque oscillators by spin pumping, inverse spin Hall, and spin Hall effects *J. Phys. D: Appl. Phys.* **117** 063907

[61] Sogandares F M and Fry E S 1997 Absorption spectrum (340–640 nm) of pure water. I. Photothermal measurements *Appl. Opt.* **36** 8699–709

[62] Yoshida C, Noshiro H, Yamazaki Y, Sugii T, Furuya A, Ataka T, Tanaka T and Uehara Y 2016 Electrical-field and spin-transfer torque effects in CoFeB/MgO-based perpendicular magnetic tunnel junction *AIP Adv.* **6** 055816

[63] Wu K, Su D, Saha R, Liu J and Wang J-P 2019 Investigating the effect of magnetic dipole–dipole interaction on magnetic particle spectroscopy: implications for magnetic nanoparticle-based bioassays and magnetic particle imaging *J. Phys. D: Appl. Phys.* **52** 335002

[64] Alamusi L H, Ning Y, Gu B, Hu N, Yuan W, Jia F, Liu H, Li Y and Liu Y 2018 Molecular dynamics simulations of thermal expansion properties of single layer graphene sheets *Mol. Simul.* **44** 34–39

[65] Jung C 1986 Poincaré map for scattering states *J. Phys. Math. Gen.* **19** 1345

[66] Žubrinić D and Županović V 2008 Poincaré map in fractal analysis of spiral trajectories of planar vector fields *Bull. Belg. Math. Soc.-Sim.* **15** 947–60

[67] Wu K, Su D, Saha R, Wong D and Wang J-P 2019 Magnetic particle spectroscopy-based bioassays: methods, applications, advances, and future opportunities *J. Phys. D: Appl. Phys.* **52** 173001

[68] Klein T, Wang Y, Tu L, Yu L, Feng Y, Wang W and Wang J-P 2014 Comparative analysis of several GMR strip sensor configurations for biological applications *Sensors Actuators Phys.* **216** 349–54

[69] Wang W, Wang Y, Tu L, Feng Y, Klein T and Wang J-P 2014 Magnetoresistive performance and comparison of supermagnetic nanoparticles on giant magnetoresistive sensor-based detection system *Sci. Rep.* **4** 5716

[70] Tu L, Wu K, Klein T and Wang J-P 2014 Magnetic nanoparticles colourization by a mixing-frequency method *J. Phys. D: Appl. Phys.* **47** 155001

[71] Cullity B D and Graham C D 2011 *Introduction to Magnetic Materials* (New York: Wiley)